Submarine channel stacking patterns controlled by the autogenic 3D kinematics of meander bends

Lemay Martin, Jean-Louis Grimaud, Isabelle Cojan, Jacques Rivoirard, Fabien Ors

Accepted Manuscript

Geological Society, London, Special Publications

Submarine channel stacking patterns controlled by the autogenic 3D kinematics of meander bends

Martin Lemay, Jean-Louis Grimaud, Isabelle Cojan, Jacques Rivoirard & Fabien Ors

DOI: https://doi.org/10.1144/SP540-2022-143

To access the most recent version of this article, please click the DOI URL in the line above. When citing this article please include the above DOI.

Received 29 April 2022
Revised 29 October 2022
Accepted 9 November 2022

Supplementary material at https://doi.org/10.6084/m9.figshare.c.6610936

Submarine channel stacking patterns controlled by the autogenic 3D kinematics of meander bends

Martin Lemay[1,2]*, Jean-Louis Grimaud[1], Isabelle Cojan[1], Jacques Rivoirard[1], Fabien Ors[1]

[1] MINES PARIS - PSL University, Centre de Géosciences, 35 rue St Honoré, 77300 Fontainebleau, France

[2] Modis, 4 rue Jules Ferry, 64000 Pau, France

ORCID ID: FA, 0000-0002-5538-7885; SA, 0000-0001-8857-8269

*Corresponding author (e-mail: martin.lemay@mines-paris.org)

Abstract:

Channel kinematics play a pivotal but underappreciated role in determining submarine meandering channel stacking patterns. A stratigraphic forward model is here applied to turbidite systems to generate synthetic stratigraphic architectures and to compare channel trajectories recorded on cross-sections with the kinematics of meander bends. Various channel stacking patterns –which may be classified into four types- are obtained from a single set of constant parameters. This variety of stacking patterns observed from one 2D section to another is thus autogenic. It is the consequence of the 3D migration of meander bends. It reflects the number of consecutive bends that have intercepted the cross-section, which depends on the channel downstream migration rate. These 3D effects alone are sufficient to explain variations of apparent migration rate and the reversal of migration direction. As a result, sigmoidal geometries can be preserved in aggrading systems without significant change of channel geometry or varying aggradation and migration rates. Finally, despite these 3D effects, stratigraphic mobility numbers still provide good constraints on bend kinematics. These results should apply to meandering rivers and other meandering systems.

Supplementary material: FLUMY model extended description, stacking pattern classification details, the methodology of channel point migration path measurements, and centreline data are available at https://doi.org/10.6084/m9.figshare.c.6610936.

The stratigraphic architecture of channelized systems is intimately linked to channel mobility, influenced by both autogenic dynamics and external forcings. Characterising these influences is necessary in both fundamental and applied stratigraphic studies. The channel dynamics of braided systems was inferred from preserved stratigraphy in laboratory experiments (e.g., Ashworth et al. 2006; Kim et al. 2010; Grimaud et al. 2017; Limaye et al. 2018). Meandering rivers are however more difficult to reproduce in the lab (Smith 1998; Howard 2009; Tal and Paola 2010; van Dijk et al. 2012) and studying the relationships between channel kinematics and preserved stratigraphy is more challenging. Sinuous to meandering channelized systems are nonetheless ubiquitous in the solar system (Baker et al. 2016), particularly in the aerial and submarine parts of Earth (e.g., Jobe et al. 2016; Ghinassi et al. 2017; Finotello et al. 2018; Lemay et al. 2020). These systems are of great interest because they are the main conduits that transfer sediment, organic carbon, and contaminants from the continental to deep-sea environments (Galy et al. 2007; Kane and Clare 2019). The deposits originating from these systems contribute to the building of reservoirs, which host natural resources (Mayall and O'Byrne 2002; Willems et al. 2020) and may be targeted for CO2 storage (Issautier et al. 2016).

The study of channel kinematics from preserved stratigraphy is eased in the submarine systems compared to the fluvial ones because of better preservation due to higher aggradation rates. Similarly, channel-fill geometries are also better described from 3D seismic data due to their large dimensions (Jobe et al. 2016; Lemay et al. 2020). Turbidite systems are thus better candidates than fluvial systems to study channel kinematics. Channel kinematics and paleoflow reconstructions of fossil systems may be analysed from 3D seismic data (Deptuck et al. 2007; Labourdette and Bez 2010; Covault et al. 2021) although many studies rely on preserved stratigraphic architectures observed on 2D cross-sections (Figure 1; e.g., Deptuck et al. 2007; Jobe et al. 2016; Mitchell et al. 2022). Horizontal and vertical channel apparent displacements recorded along cross-sections define a channel stacking pattern (Clark and Pickering 1996; Mayall and O'Byrne 2002; Deptuck et al. 2007; Labourdette and Bez 2010; McHargue et al. 2011; Sylvester et al. 2011; Macauley and Hubbard 2013). A change of channel stacking pattern is most often interpreted as a change in channel dynamics and/or flow properties (Figure 1; Deptuck et al. 2007; McHargue et al. 2011). Sylvester et al. (2011) however showed that such complexity is inherent to meandering systems and that the resulting stratigraphic architectures, for instance in submarine valleys, may vary without external change.

Some studies also measured paleo-channel kinematics from channel stacking patterns observed within cross-section data (Jobe et al. 2016; Mitchell et al. 2022). These studies rely on the ratio between channel lateral (*Lc*) over vertical (*La*) recorded displacements during a given time span normalised by channel dimensions (Jerolmack and Mohrig 2007; Jobe et al. 2016). This index is known as the stratigraphic mobility number $\mu=(Lc/B)/(La/H)$ where *B* and *H* are channel width and depth, respectively. However, channel motion also led to sediment reworking (e.g., Grimaud et al. 2022) so inferring channel mobility from the stratigraphic mobility number alone is not straightforward. There is still room for improving our understanding of the relationships between channel kinematics and preserved stratigraphic architectures to correctly interpret stacking patterns.

In this study, aggrading meandering channels were simulated in a turbidite environment using the FLUMY stratigraphic forward model. The variability of channel stacking patterns generated from a single set of constant parameters -and recorded on cross-sections orthogonal to meander bends- is compared to the actual dynamics of individual bends. To that purpose, channel centrelines were extracted at regular time steps (i) to analyse their successive positions and (ii) to construct their stratigraphic record.

Method

Description of the model

The FLUMY model aims at building facies 3D blocks at the reservoir scale by simulating the evolution of a meandering channelized system. In this study, it was used to simulate a sinuous submarine leveed-channel system in an aggrading context. The simulated processes were the meandering channel migration, avulsion, and aggradation of the leveed-channel complex (sensu Abreu et al. 2003). The model was initially developed for meandering fluvial systems (Lopez 2003; Cojan et al. 2011; Koneshloo et al. 2017; Grimaud et al. 2022) and extended to turbidite systems (Lemay 2018; Lemay et al. 2019) based on observed similarities between the two environments (Imran et al. 1999; Sylvester et al. 2011; Lemay et al. 2020). A summary of the turbidite model is provided in the Supplementary Material.

Channel lateral migration adapted to the submarine environment. In FLUMY, the channel was modelled as a series of nodes -a centreline- moving across the domain of simulation. The migration algorithm (see Supplementary Material for details) computed the channel displacements by solving depth-averaged Saint-Venant equations, which generated lateral accretion deposits (LADs) (Abreu et al. 2003; Arnott 2007; Dykstra et Kneller 2009; Hansen et al. 2017) and bend cutoffs (Deptuck et al. 2007; Sylvester and Covault 2016; Wiles et al. 2017). The equations governing channel migration were essentially the same as in the fluvial version, i.e., assuming that the channel migration was proportional to the flow velocity perturbation along the outer bank (Figure 2; e.g., Imran et al. 1999; Grimaud et al. 2022). This meander migration model resulted in a maximum migration rate occurring downstream maximum curvature -i.e., sub-resonant conditions- (Imran et al. 1999; Seminara 2006; Figure 2), which favoured downstream migration of meander bends. Compared to the fluvial one, the turbiditic mode included: (i) a steeper basin slope, (ii) larger channel dimensions and aspect ratio (B/H), and (iii) the densiometric Froude number that takes into account sediment concentration (10% here) and submerged specific gravity (Imran et al. 1999).

According to Imran et al. (1999), this model of channel migration accounted for subcritical dilute turbidity currents that flow on gentle slopes during hours or days with low variations of sediment budget. Such channelized currents are most likely to be found downstream of a canyon (Pirmez and Imran 2003; Traer et al. 2018) where leveed-channel systems are the most developed (Lemay et al. 2020). Previous studies showed that these kinds of submarine channel evolution models could reproduce realistic planform morphologies and associated stratigraphic architectures (Imran et al, 1999; Sylvester et al. 2011; Covault et al. 2016; Lemay 2018).

Aggradation and avulsion. The aggradation model accounted for in-channel sedimentation, flow overspill and flow stripping (see Supplementary Material). Pelagic sedimentation was not simulated in this study. The user set channel mean aggradation rate -i.e., in-channel sedimentation rate.

Overflow spilling was computed using lateral diffusion of flow away from the channel that yielded an exponential decreasing aggradation rate with distance. Flow overspill was higher along the outer bank than the inner bank due to flow superelevation (Imran et al. 1999). This model reproduced most of the behaviours observed from experiments and modern submarine systems: (i) identical aggradation rate between channel floor and levee crests for straight reaches (Kane et al. 2008), (ii) flow superelevation leading to thicker outer levee compared to inner levee for curved reaches (Komar 1969; Peakall et al. 2000; Straub and Mohrig 2008) and (iii) exponential decrease of levee thickness away from the channel (e.g., Skene et al. 2002; Birman et al. 2009; Nakajima and Kneller 2013).

In this study, regional avulsions (upstream of the simulation domain) were generated following a user-defined avulsion period when a new entry point was randomly chosen along the upstream side of the simulation domain. A new channel path was then determined following a random walk along the steepest slope from the entry point, which resulted in the abandonment of the previous channel path (Figure 3).

Parameters used in the study. A simple scenario with fixed parameters was run in this study. The formation of 9 submarine channel belts was simulated (Figure 3). Each channel belt resulted from the migration and aggradation of a single channel -represented by its centreline- starting from a nearly straight path until the avulsion of the whole path. Simulated channel belts corresponded to the stage 1 described by Morris et al. (2022) where channel sinuosity and belt width rapidly increased until the first bend cutoffs.

Chosen parameters corresponded to a median submarine leveed-channel system according to Lemay et al. (2020). Channel was 1200 m wide (bank to bank), 50 m deep (maximal depth), and the input maximal wavelength was 4200 m. Erodibility coefficient was spatially constant and equaled 2.10^{-8}. Avulsion period was set to 4,000 iterations, which corresponds to the time of the first cutoffs. Simulated channel belts were 5-10km wide and average channel sinuosity before avulsion was about 2.25, which is in the range of channel-belt width and sinuosity measurements in natural systems (Deptuck et al. 2007; Morris et al. 2022). Channel aggradation intensity was set to 2 m every 100 iterations, which yields 78 m of total aggradation -i.e., 1.56 times channel depth- by the end of each channel-belt evolution. Deposits were stored in a regular pillar grid 100 km cross-stream (i.e., orthogonal to the global flow direction) by 50 km downstream with a grid resolution of 200x200 m² (Figure 3). Cell dimensions were set to be at least twice smaller than the channel width to ensure an accurate description of channelized deposits. Note that the simulation did not aim at simulating a particular submarine channel system but at reproducing realistic channel kinematics and resulting deposits.

It was assumed that an iteration in the model corresponded to major turbidity events that occurred every 1-2 years (Paull et al. 2018; Brocheray et al. 2013). Channel belt activity duration was thus around 4,000-8,000 years. According to the exponential decreasing rate of overbank accumulation away from the channel -i.e., 5.8 times the channel width- the mean aggradation rate in the simulated domain was 1.7-3.4 m/kyr. The mean channel migration rate was 0.32-0.65 m/yr and channel aggradation rate was around 10-20 m/kyr, which yields a channel mobility number (*sensu* Jerolmack and Mohrig 2007) around 1.3.

Meander bend kinematics characterization

Channel displacements and kinematics were analysed by comparing the actual dynamics of individual bends with the record along sections across meander bends. First, the successive positions of the nine centrelines through time were extracted and segmented (Figures 4 and 5). Second, 187 synthetic cross-sections were constructed from the intersections of these successive centrelines (Figure 6). Bend migration (Figure 7) and horizontal and vertical displacements of the centrelines along these sections were measured (Figure 8). Finally, the stratigraphic mobility numbers were compared with bend kinematics (Figure 9).

Centreline extraction. Channel centrelines were extracted every 100 iterations during the simulation, resulting in 40 successive positions for each of the 9 centrelines (Figures 4 and 5). Extracted centrelines were resampled every 50 m based on a parametric spline function and then smoothed using a Savitzky-Golay filter (Savitzky and Golay, 1964) with a third-order polynomial and a window length scale approximately equal to half the meander wavelength (see also Lemay et al. 2020). Channel point properties (i.e., flow height, superelevation, mean velocity, velocity perturbation, etc.) were linearly interpolated to resampled points and the curvature was computed from the previous and next points.

Channel points of the 9 evolving centrelines were tracked back through time using dynamic time warping algorithm (*dtw 1.3.0* Python package from Giorgino (2009) - see also Sylvester et al. 2019; Figure 5). The algorithm minimises the cumulative cost to "link" each channel point of the centreline at *t*, to each point of the centreline at *t-1*. The cost function used here included channel point Euclidean distance and differences of both curvature and velocity perturbations along the outer bank. Each of these components was normalised by its maximum value and accounted for a third of the cost function. The average migration vector corresponded to bend migration -conversely to Sylvester et al. 2019 who measured bank migration- which was more consistent for comparison with the 2D channel migration along geological sections. The average bend migration indeed tracked the migration of multiple points along the channel (Figure 6) since it was defined as the average of the migration paths of all the points of the bend between upstream and downstream inflection points (Figure 7). The bend mobility number was computed as the ratio between average bend migration and channel total aggradation similarly to the stratigraphic mobility number.

The consecutive channel bends were identified using changes of curvature from positive (blue) to negative (red) values or inversely (Figure 4). Curvature of each channel-point was smoothed using a Savitzky-Golay filter to prevent discretization effects. Inflection points and apexes were defined along the smoothed centreline as null and maximum curvature points, respectively (Figure 4).

Construction of synthetic geological cross-sections. Cross-sections were manually defined in the 9 channel belts to occupy locations across meander bends comparable to those obtained from field surveys or seismic data (e.g. Deptuck et al. 2007; Jobe et al. 2016; Figure 4). Sections that only crossed once each set of the 40 successive centrelines were selected, giving a total of 187 cross-sections from the 9 simulated channel belts. Figure 5 shows the successive centreline positions for a selection of four typical cross-sections (Figure 6). On each cross-section, the 40 successive positions of the centreline are indicated with a colour code: bends with positive curvature were plotted in blue, and those with negative curvature in red (Figure 6).

Channel kinematics from average bend migration. The kinematics of the individual bends intersecting the sections were computed from the centreline evolution through time. The average

bend migration path was computed as the mean of migration paths of all points between upstream and downstream inflection points from the youngest centreline (Figure 7; see Supplementary Material). The average bend migration path was projected on the given cross-section to be compared to the geological record. The total belt-averaged bend migration (*Mig*) -i.e., the length of the average bend migration path from the first to the last centreline- was measured from the first to the last centreline positions. The orthogonal (D_1) and parallel (D_2) components to the cross-section were then computed. These measurements were normalised by channel width and are represented in Figure 7.

Channel kinematics inferred from cross-sections.

Belt-averaged kinematics inferred from total displacement. Vertical (*La*) and horizontal (*Lc*) apparent displacements of the channels were first measured from the cross-sections in two ways. The subscript *w* was used when measuring the displacement along the whole path starting from the oldest to the youngest channel position (Lc_w and La_w), and the subscript *f* when considering the displacement along the final migration phase since the last position where the direction of horizontal displacement changed (Lc_f and La_f; Figure 8). Lateral displacement was normalised by channel width ($Lc_{w,\,norm}$, $Lc_{f,\,norm}$) and vertical displacement by channel depth ($La_{w,\,norm}$, $La_{f,\,norm}$; Figures 8a to 8c). Note that $La_{w,\,norm}$ here was equal to 1.56 since it corresponded to the total aggradation of the channel (78 m -i.e., 39 aggradation steps of 2 m) divided by the channel depth (i.e., 50 m). Two mobility numbers ($\mu_f = Lc_{f,\,norm}/La_{f,\,norm}$ and $\mu_w = Lc_{w,\,norm}/La_{w,\,norm}$) were defined from these measurements similarly to the belt-averaged stratigraphic mobility number from Jobe et al. (2016). Results were compared with the belt-averaged bend mobility number M_{bend} computed from the total belt-averaged bend migration and vertical displacement -i.e., from the first and the last centrelines (Figure 9).

Local kinematics inferred from incremental displacements. Figure 10 shows average bend migrations every 100 iterations in comparison to channel horizontal displacements recorded along the corresponding cross-sections, both normalised by the channel width *B*. Negative and positive channel displacements accounted for leftward and rightward displacements in cross-sections, respectively, and changes of bends were identified by colour coding the curvature in blue (positive) or red (negative).

Results and interpretations

Centreline migration

Observed planform dynamics showed contrasted channel migration patterns despite constant and steady forcing parameters (Figure 5). The main meander transformation modes, which included expansion (e.g., bend 6.5 in Figures 5a and 5b), translation (e.g., bend 8.5 in Figures 5c and 5e) and rotation (e.g., bend 8.6 in Figures 5c and 5e; Daniel 1971; Jackson 1976), were reproduced here. These modes mainly reflected the combined effects of the initial centreline geometry with the self-organisation of the channel path, i.e., related to interactions with neighbouring bends. In map view, channels evolved from a nearly straight path (dark purple line) to an increasingly sinuous one (yellow line; Figure 5) resulting from the combination of downstream and cross-stream migrations. Mean bend downstream and cross-stream migrations were 0.90 and 1.13 times channel width, respectively.

Each synthetic cross-section most often intersected up to 3 consecutive bends. It resulted in one or successive phases of migration recorded by the section. For instance, the sections crossing bends 6.5 (Figure 5b) and 8.6 (Figures 5d-e) recorded a single direction of migration but for bend 8.6 the first phase showed nearly no channel lateral migration. The sections crossing bend 6.14 and 2.9 recorded 2 (Figure 5g-h) and 3 (Figure 5j-l) phases of migration in opposite directions respectively.

Channel stacking patterns

Extracted cross-sections displayed various stratigraphic architectures and stacking patterns (Figure 6). Channel trajectories varied from concave-up to convex-up geometries (Figure 6). Channel stacking patterns were divided into 4 types according to channel apparent trajectory along the cross-sections (Figure 6; see Supplementary Material). Type 1 (23% of the sections) corresponded to a one-swing migration pattern, i.e., apparent migration in a unique direction. Type 2 (11% of the sections) showed the first phase with nearly no lateral migration followed by a one-swing migration phase, i.e., also characterised by a unique direction of significant lateral displacements. Type 3 -the predominant pattern (52%)- recorded two-swings migration, i.e., there was the first phase with an apparent migration in a given direction, then a second phase with an apparent migration in the other direction. Type 4 (14% of the sections) showed two or more migration directions.

The four endmembers introduced here were useful to illustrate the variability observed from one cross-section to the next. However, there was a continuum between them. Indeed, channel trajectory changes visible on the sections originated from changes in the apparent lateral migration rate and direction only. One must keep in mind that the channel aggradation rate was constant (i.e., 2 m every 100 iterations) during the building of each channel belt. It was also observed that increased stacking patterns complexity was due to an increasing number of bends intersecting the cross-section (which increased from type 1 to 4) (Figure 6). Importantly, the change of bends -i.e., change of colour in Figure 6- did not coincide with a change in apparent migration direction.

Bend displacements

Total belt-averaged bend migration varied from 0.2 to 3.0 times channel width, with a slight decrease from type 1 (0.75-3.0, median: 1.7) to type 4 (0.3-2.3, median: 1.5; Figure 7a). In detail, median values of migration components orthogonal and parallel to the sections varied according to the stacking pattern (Figures 7b and 7c). Normalised migration orthogonal to the section ranged from 0 to 2.8 and slightly increased from type 1 (median 0.8) to types 2 and 3 (median: 0.9) and type 4 (median: 1.0) (Figure 7b). Bend normalised migration parallel to the sections varied from 0 to 2.6 and decreased from type 1 to type 4 (median 1.3, 1.2, 1.0 and 0.9, respectively; Figure 7c). Note that apex migration path was also measured and showed good correlation with average bend migration measurements (see Supplementary Material).

Channel displacements recorded on cross-sections

Channel displacements recorded on cross-sections were contrasted and ordered according to stacking pattern complexity (Figure 8). Overall, channel lateral displacement along geological cross-sections varied from 0.1 to 3.5 times the channel width. It decreased from type 1 to types 2, 3 and 4, i.e., independently of the methodology of measurement used (i.e., considering the whole path or only the final one) (Figures 8a and 8b). Types 1 and 2 displayed very similar distributions with

median values for both methodologies around 2.4 and 2.0, respectively. Horizontal displacements of types 3 and 4 measured from the last migration phase (medians: 1.8 and 1.6, respectively) were slightly higher than the one obtained from the whole path (medians of 1.5 for both and lower extremum). Vertical displacements measured on cross-sections from the last phase of migration decreased from type 1 -equal to the total vertical displacement from the whole path for all sections- to type 4 (median 0.8; Figure 8c). Hence with increasing complexity, recorded horizontal migration decreased independently of the methodology used. The ability to measure aggradation from the last phase of migration also decreased as a function of complexity.

Bend versus stratigraphic mobility numbers

Belt-averaged mobility numbers measured from bend dynamics (M_{bend}) or cross-sectional records (μ) ranged from 0 to 4.6 (Figure 9). The latter were greater than the former. In detail, M_{bend} slightly decreased from type 1 to type 4 -although median values are around 1.0 for all types- similarly to μ_w -median values around 1.6 and 1.3 for types 1 and 2, and 1.0 for types 3 and 4 (Figure 9d). Conversely, μ_f increased from type 1 (median: 1.5) to type 4 (median: 2.0; Figure 9e). Despite discrepancies in their distributions, M_{bend} and μ values were correlated and the correlation is better for μ_w than μ_f (*p-value* < 0.05; R^2=0.52 and 0.35 for μ_w and μ_f respectively; Figures 9a and 9b). On average, both μ_w and μ_f measurements overestimated M_{bend} values for types 1 and 2 (Figures 9a and 9f; Table 1) while only μ_f overestimated M_{bend} values for types 3 and 4 (Figures 9b and 9f; Table 1).

Local apparent channel displacements versus bend displacements

Local displacements from all stacking pattern types showed that average bend migration varied much less with time than channel displacements recorded on the cross-sections (Figure 10). Indeed, normalised migration from average bend displacements was typically below 0.1 and showed little variability. On the contrary, normalised migration from the cross-sectional record suggested stronger and sharper variations as typified by stacking patterns 3 to 4 (Figures 10c and 10d) with rapid oscillations and values up to 0.22. These cycles corresponded to the migration phases described in Figures 5 and 6.

As shown previously, the increasing pattern complexity observed from type 1 to 4 was related to an increasing number of meander bends intersecting the cross-section (Figure 5), which could also be tracked on cross-sections in Figure 10. A colour code similar to that used in Figures 3 and 6 was used to show the changes in bend (red: negative curvature and blue: positive curvature; Figure 10). Interestingly, a migration maximum was observed in most cases right after a change of bend occurred (Figure 10), e.g., section 6.5 which recorded two consecutive bends, sections 8.6 and 6.14 recorded three bends, and section 2.9 recorded four bends (Figures 6 and 10).

Discussion

In this study, submarine meandering channel kinematics were compared with channel stacking patterns and recorded kinematics inferred from cross-sections along an aggrading succession produced by a stratigraphic forward modelling tool, FLUMY.

Autogenic channel stacking pattern variability

Channel stacking pattern is a key element for submarine channel interpretations in terms of channel evolution history, changes of extrinsic or intrinsic parameters such as flow properties, and highly impact reservoir connectivity (Clark and Pickering 1996; Mayall and O'Byrne 2002; Deptuck et al. 2007; Macauley and Hubbard 2013; Morris et al. 2022). This study shows that inside a single channel-complex (sensu Abreu et al. 2003) a large variety of recorded channel stacking patterns may be observed without changes in external forcings. They are thus the result of the autogenic meandering process. Hence, channel stacking changes -measured in this study (Figures 3 and 6) and also in natural systems (Figure 1; Clark and Pickering 1996; Mayall and O'Byrne 2002; Deptuck et al. 2007; Labourdette and Bez 2010)- can elementarily be considered as such when interpreting 2D cross-sections. Indeed, stacking pattern complexity increases with the increasing number of bends being intersected by the cross-section (Figures 5 and 6). This trend is further favoured by high downstream migration rates (Figure 10). Importantly, these results suggest that changes in the channel stacking pattern alone are not sufficient to discriminate between different channel complexes, nor to invoke changes of flow properties, which Sylvester et al. (2011) also pointed out: 'Many, if not most, submarine channel systems have a simpler history of channel incision, aggradation, and flow variability than previously thought'.

Results from this study highlight the limits of using changes in stacking pattern (migration direction and rate) to discriminate between channel complexes on large-scale cross-sections (e.g., Macauley and Hubbard 2013). Indeed, cross-sections do not record the displacement of a single channel point (e.g., bend apex) but rather successive points along the curved centreline through time (Figures 5 and 6) as illustrated by changes of channel curvature (Figure 10). Thus, depending on the chronology of which part of the bend intersects the cross-section, various patterns may emerge, particularly as the bend migration rate is driven by curvature (e.g., Sylvester et al. 2019). Perhaps an alternative way to discriminate between on one side intrinsic and continuous, or on the other side extrinsic and discontinuous evolution would be to look at grain size. In the example of a two-swings stacking pattern (type 3) where channel migration direction changes, an externally forced transition from a sinuous to a straighter channel due to an upstream avulsion would be associated with a sharp coarsening of deposits while an autogenic change in stacking pattern due to continuous channel migration would not show a too sharp transition in grain size.

Downstream migration controls change in stacking patterns

This study highlights that stacking pattern complexity reflects the locally increased downstream migration rate of meander bends (Figures 5 and 7b). Indeed, 2D sections record the migration component parallel to the direction of these sections but miss the migration component orthogonal to them. Consequently, the apparent migration observed on 2D sections arises from two facts: (i) it is not the average bend migration path nor the migration path of a single channel point that is captured but that of any part of the channel intersecting the cross-section, and (ii) several bends -not just one- may be recorded along the section. In other words, 2D data are incomplete and this is the reason why interpretations of channel dynamics should rely on 3D data when it is possible. This is particularly the case in systems where channel belts are more mature, where repeated bend life cycles intersected cross-sections thus creating more complex stacking patterns (Morris et al. 2022). The same is expected in confined systems such as valleys where the downstream migration rate is enhanced and patterns are dominated by vertical aggradation (e.g., Labourdette and Bez 2010; Macauley and Hubbard, 2013; Lemay et al., 2019).

However, although the downstream migration is not recorded in cross-sections, changes in stacking patterns reflect the number of bends intersected by the cross-section, which may also reflect the bend downstream translation rate (Figure 7b). This can be estimated roughly by counting the number of direction changes on a cross-section plus one (i.e., Figure 6). One could also try to reconstruct channel local migration (i.e., Figure 10) using aggradation height instead of time-based on high-resolution cross-sections and to identify migration maxima. However, changes in the direction and rate of migration are not always easy to identify. Identifictions depend on the quality of the outcrop or seismic data and the amalgamation of channels that is enhanced in low aggradational systems. Another strategy could therefore be to use backward modelling for reconstructing the migration history of the channel (e.g., Labourdette and Bez 2010; Parquer et al. 2020).

From convex-up to concave-up channel trajectories

Channel stacking patterns change vertically along the cross-sections, displaying convex-up and/or concave-up trajectories (Figure 6). These geometries are most often present in the simulated sections and alternate most of the time for bends with significant downstream migration (Figures 7b). They result in variations of apparent migration rate, increasing then decreasing periodically (Figure 10). Apparent migration variations observed here can be explained as follows (Figure 11). Convex-up trajectories correspond here to phases when the apparent migration rate increases from 0 to a maximum value (Figure 10). Null apparent migration values are most often observed when a bend apex crosses the section (Figure 11). The maximum apparent migration value is reached slightly after an inflection point crosses the section -i.e., change of colour in Figures 6 and 10 (Figure 11). Indeed, during that time lapse channel becomes more and more parallel to the section at the crossing point. Every increment of downstream migration thus yields a larger apparent migration step. Once the inflection point crosses the section, apparent migration starts to decrease (Figures 6 and 10) since the channel direction gets more and more orthogonal to the section (Figure 11). The maximum of orthogonality between the channel and the section is reached when the apex crosses the section and results in a null apparent migration rate. This mechanism generates a sigmoidal apparent channel trajectory on 2D sections (Figure 11), and we argue that it corresponds to the autogenic meander kinematics and geometrical 3D effects happening in systems with significant downstream migration.

Convex-up trajectories are rarely observed in natural systems -particularly at the inception of channel belts- contrary to the simulation. Two effects may combine to explain this difference: i) submarine channel aggradation rate is very low at the beginning of bend migration (Jobe et al. 2016) and ii) channel may progressively deepen by incision during the first phase of channel-belt development (de Leeuw et al. 2016). In both cases, these effects result in reworking previous deposits which prevents preserving the low migration phase. Conversely, concave-up geometries have been reported for decades in submarine but also in fluvial systems (Peakall et al. 2000; Sylvester et al. 2011; Jobe et al. 2016; Morris et al. 2022). Their origin remains debated, and they could arise from external forcings such as tectonic control, changes in sediment supply and/or equilibrium profile (Kneller 2003; Hodgson et al. 2011; Covault et al. 2021), or be self-formed. They are observed in most meander bend cross-sections, which suggests an autogenic process such as: (i) change of helical flow structure during bend expansion (Dorrell et al. 2014; Azpiroz-Zabala et al. 2017), and/or (ii) progressive levee growth and levee superelevation (Peakall et al. 2000; Jobe et al.

2016). Channel trajectories much more concave than those created in the simulation were observed in natural systems and called “hockey stick geometries”. They suggest an increasing aggradation rate combined with a decreasing lateral apparent migration rate (Jobe et al. 2016). This study does not address the exact formation process of hockey stick geometries, but the results suggest that at least part of their concave-up geometry may arise from autogenic meander kinematics and geometrical 3D effects.

Kinematic vs. stratigraphic channel mobility numbers

This study highlights that channel kinematics should be measured from 3D data, which now resolve individual channel locations (Covault et al. 2021; Morris et al. 2022), to best characterise channel mobility. Interestingly, bend mobility measured in this study from the 3D dataset was 1.3 times lower than theoretical average channel mobility. The discrepancy comes from channel migration measurements that are lower than the theoretical mean value. It may be interesting to compare with the bend mobility number measured from bank migration (Sylvester et al. 2019). Bend mobility is nevertheless considered in the following as the reference value. Bend mobility can indeed be measured on natural systems from 3D data whereas theoretical channel migration and aggradation rates cannot be directly inferred from stratigraphic data due to the stratigraphic filter (Schumer et al. 2011; Grimaud et al. 2022).

In many places, however, only 2D data are available. Although kinematics measured from cross-sections generally differ from actual channel kinematics (see previous sections), they are nevertheless correlated (Figure 9). In particular, the belt-averaged bend mobility M_{bend} is most often overestimated using stratigraphic 2D data, but the best estimation comes from measurements of the whole channel path μ_w (Figures 9a and 9f; Table 1). In detail, μ_w overestimates M_{bend} for types 1 and 2 while it may either overestimate or underestimate M_{bend} for types 3 and 4 (Figures 9a and 9f; Table 1). μ_f always overestimates M_{bend} for all types and the discrepancy increases with channel stacking pattern complexity (Figure 9f; Table 1). Bend mobility is most often overestimated because bend migration is averaged over all channel points of the bend going in various directions (Figure 5). Indeed, the average bend migration path is shorter than most of its individual channel point migration paths (Figure 5). So, even in the case where the section is parallel to channel points migration direction -e.g., second half of bend 6.5 migration (Figure 5b)- measured migration is still higher than average bend migration (Figure 10a). In this last case, the apparent migration recorded in the section during the second half of meander-belt development best fits with the apex migration. Although the stratigraphic mobility numbers μ_f and μ_w are not direct measures of average bend mobility, they are still useful metrics that provide upper limits.

Transposition to other natural systems

The simulation used in this study was generated with FLUMY calibrated for submarine channels. The model reproduces the main components of channel kinematics including channel aggradation, bend lateral migration (swing) and downstream migration (sweep) as observed in any natural meandering systems (Deptuck et al. 2007; Ghinassi et al. 2017; Sylvester et al. 2021; Morris et al. 2022). Therefore, the vertical stacking and basic modes of planform transformation of meander bends (i.e., expansion, translation, rotation; Daniel 1971; Jackson 1976) observed in all types of systems are reproduced by the model.

In this study, the absolute values of migration and aggradation rates were however not precisely calibrated for turbidite systems, which led to simulated mobility numbers intermediate between submarine and fluvial systems (Jobe et al. 2016). This is currently not an issue as this study focused on their relative value evolution during channel-belt development. More generally, similarities of dynamics (Lemay et al. 2020) and stacking patterns are suggested for fluvial and submarine channels, with the noticeable difference of higher aggradation rate relative to migration rate in the latter domain (Jobe et al. 2016). Results may therefore also apply to meandering alluvial rivers, tidal channels, and other meandering systems in the solar system, although absolute values of mobility numbers are to be expected in relation to changes in the mode of bend development in these systems.

Conclusion

A large variety of channel stacking patterns are obtained from a single set of constant parameters in a simulation of meandering submarine channels. They can be classified into four stacking pattern types: (1) One-swing, (2) No migration then one-swing, (3) Two-swings and (4) Multiple swings. The whole complexity observed in the simulated cross-sections of aggrading submarine channels results from autogenic kinematics of meander bends and 3D geometrical effects. Increase in stacking pattern complexity on cross-sections reflects the number of consecutive bends that have been intercepted by the cross-section, which depends on the downstream migration rate of meander bends. The complexity observed on two-dimensional stratigraphic sections is therefore the consequence of the three-dimensional migration of meander bends, which are imperfectly intersected by the sections. Meander migration results in sigmoidal geometries that can be observed in aggrading submarine systems with no significant change of channel geometry or varying aggradation and migration rates due to other processes. Finally, a comparison between stratigraphic and bend mobility numbers shows that they are correlated despite discrepancies increasing with channel stacking pattern complexity. These results might apply to meandering rivers and other meandering systems.

Acknowledgements

The results presented in this paper are part of the first author's PhD thesis. This work has been supported by the FLUMY Research Program Armines / MINES PARIS. The FLUMY Research Program sponsors, ENGIE (now Neptune Energy) and ENI, are acknowledged for financial support and fruitful discussions. Julien Michel is thanked for discussions and the revision of preliminary versions of the manuscript, and we are grateful for the reviews of Zoltan Sylvester, Neal Auchter and Jacob Covault which greatly improved the manuscript.

Author contributions

Funding

Data availability

References

Abreu, V., Sullivan, M., Pirmez, C., and Mohrig, D., 2003. Lateral accretion packages (LAPs): an important reservoir element in deep water sinuous channels. *Marine and Petroleum Geology,* 20 (6–8), 631–648. https://doi.org/10.1016/j.marpetgeo.2003.08.003.

Arnott, R. W. C. 2007. Stratal architecture and origin of lateral accretion deposits (LADs) and conterminuous inner-bank levee deposits in a base-of-slope sinuous channel, lower Isaac Formation (Neoproterozoic), East-Central British Columbia, Canada. *Marine and Petroleum Geology,* 24 (6-9), 515-528. https://doi.org/10.1016/j.marpetgeo.2007.01.006.

Ashworth, P. J., Best, J. L., & Jones, M. A. 2007. The relationship between channel avulsion, flow occupancy and aggradation in braided rivers: insights from an experimental model. *Sedimentology,* 54(3), 497-513. https://doi.org/10.1111/j.1365-3091.2006.00845.x.

Azpiroz-Zabala, M., Cartigny, M.J., Sumner, E.J., Clare, M.A., Talling, P.J., Parsons, D.R., and Cooper, C., 2017. A general model for the helical structure of geophysical flows in channel bends. *Geophysical. Research. Letters.* 44 (23). https://doi.org/10.1002/2017GL075721.

Baker, E., Gaill, F., Karageorgis, A., Lamarche, G., Narayanaswamy, B., and Parr, J., et al. 2016. Offshore mining industries. *In: The First Global Integrated Marine Assessment. World Ocean Assessment I,* United Nations (UN): New York, NY, USA

Birman, V. K., Meiburg, E., and Kneller, B. 2008. The shape of submarine levees: exponential or power law? *Journal of Fluid Mechanics,* 619, 367-376. https://doi.org/10.1017/S0022112008004862.

Brocheray, S., Cremer, M., Zaragosi, S., Schmidt, S., Eynaud, F., Rossignol, L., and Gillet, H. 2014. 2000 years of frequent turbidite activity in the Capbreton Canyon (Bay of Biscay). *Marine Geology,* 347, 136-152. https://doi.org/10.1016/j.margeo.2013.11.009

Clark, J.D., and Pickering, K.T., 1996. *Submarine Channels: Processes and Architecture*. Vallis Press, London, pp. 232p

Cojan, I., Rivoirard, J., Ors, F., and Renard, D. 2011. New Method for an Easy Use of Stochastic Process-Based Models Such as FLUMY to Reproduce a Fluvial Meandering Reservoir. *In: 73rd EAGE Conference and Exhibition-Workshops* 23-27 May 2011, Vienna, Austria. pp. cp-239 https://doi.org/10.3997/2214-4608.20144712

Covault, J.A., Sylvester, Z., Hubbard, S.M., Jobe, Z.R., and Sech, R.P., 2016. The stratigraphic record of submarine-channel evolution. *Sedimentary. Research*. 14 (3), 4–11. https://doi.org/10.2110/sedred.2016.3

Covault, J.A., Sylvester, Z., Ceyhan, C., and Dunlap, D.B., 2021 Giant meandering channel evolution, Campos deep-water salt basin, Brazil: *Geosphere*, v. 17, no. X, p. 1– 21, https://doi.org/10.1130/GES02420.1.

Daniel, J.F. 1971 Channel movement of meandering Indiana streams. *U.S. Geol. Surv. Prof. Pap.*, 732-A, 18 pp.

Deptuck, M.E., Sylvester, Z., Pirmez, C., and O'Byrne, C., 2007. Migration–aggradation history and 3-D seismic geomorphology of submarine channels in the Pleistocene Benin major Canyon, western Niger Delta slope. *Marine and Petroleum Geology,* 24 (6–9), 406–433. https://doi.org/10.1016/j.marpetgeo.2007.01.005.

Dorrell, R.M., Darby, S.E., Peakall, J., Sumner, E.J., Parsons, D.R., and Wynn, R.B., 2014. The critical role of stratification in submarine channels: implications for channelization and long runout of flows. *Journal of Geophysical Research: Oceans* 119 (4), 2620–2641. https://doi.org/10.1002/2014JC009807.

Dykstra, M., and Kneller, B. 2008. Lateral accretion in a deep-marine channel complex: implications for channellized flow processes in turbidity currents. *Sedimentology*, 56(5), 1411-1432. https://doi.org/10.1111/j.1365-3091.2008.01040.x.

Finotello, A., Lanzoni, S., Ghinassi, M., Marani, M., Rinaldo, A., and D'Alpaos, A. 2018. Field migration rates of tidal meanders recapitulate fluvial morphodynamics. *Proceedings of the National Academy of Sciences*, 115(7), 1463-1468. https://doi.org/10.1073/pnas.1711330115

Galy, V., France-Lanord, C., Beyssac, O., Faure, P., Kudrass, H., and Palhol, F., 2007. Efficient organic carbon burial in the Bengal fan sustained by the Himalayan erosional system. *Nature* 450 (7168), 407. https://doi.org/10.1038/nature06273.

Giorgino, 2008. Computing and Visualizing Dynamic Time Warping Alignments in R: The dtw Package. J. Stat. Soft., 31 https://doi.org/10.18637/jss.v031.i07.

Ghinassi, M., D'alpaos, A., Gasparotto, A., Carniello, L., Brivio, L., Finotello, A., ... and Cantelli, A. 2018. Morphodynamic evolution and stratal architecture of translating tidal point bars: Inferences from the northern Venice Lagoon (Italy). *Sedimentology*, 65(4), 1354-1377. https://doi.org/10.1111/sed.12425

Grimaud, J. L., Paola, C., and Ellis, C. 2017. Competition between uplift and transverse sedimentation in an experimental delta. *Journal of Geophysical Research: Earth Surface*, 122(7), 1339-1354. https://doi.org/10.1002/2017JF004239

Grimaud, J.L., Ors, F., Lemay, M., Cojan, I., and Rivoirard, J., 2022. Preservation and completeness of fluvial meandering deposits influenced by channel motions and overbank sedimentation. *Journal of Geophysical Research: Earth Surface, e2021JF006435.* https://doi.org/10.1029/2021JF006435

Hansen, L., Janocko, M., Kane, I., and Kneller, B. 2017. Submarine channel evolution, terrace development, and preservation of intra-channel thin-bedded turbidites: Mahin and Avon channels, offshore Nigeria. *Marine Geology*, 383, 146-167. https://doi.org/10.1016/j.margeo.2016.11.011.

Hodgson, D.M., Di Celma, C.N., Brunt, R.L., and Flint, S.S., 2011. Submarine slope degradation and aggradation and the stratigraphic evolution of channel–levee systems. *Journal of the Geological Society,* 168 (3), 625–628. https://doi.org/10.1144/0016-76492010-177.

Howard, A. D. 2008. How to make a meandering river. *Proceedings of the National Academy of Sciences*, 106(41), 17245-17246. https://doi.org/10.1073/pnas.0910005106

Imran, J., Parker, G., Pirmez, C., 1998. A nonlinear model of flow in meandering submarine and subaerial channels. *Journal of Fluid Mechanics*, 400, 295–331. https://doi.org/10.1017/S0022112099006515.

Issautier, B., Viseur, S., Audigane, P., Chiaberge, C., and Le Nindre, Y. M. 2016. A new approach for evaluating the impact of fluvial type heterogeneity in CO2 storage reservoir modelling. *Comptes Rendus Geoscience*, 348(7), 531-538. https://doi.org/10.1016/j.crte.2015.06.006

Jackson, R.G. 1976, Depositional model of point bars in the lower Wabash River. *Journal of Sedimentary Petrology*, 46, 579–594. https://doi.org/10.1306/212F6FF5-2B24-11D7-8648000102C1865D

Jerolmack, D. J., and Mohrig, D., 2007. Conditions for branching in depositional rivers. *Geology*, 35(5), 463-466. https://doi.org/10.1130/G23308A.1.

Jobe, Z.R., Howes, N.C., and Auchter, N.C., 2016. Comparing submarine and fluvial channel kinematics: implications for stratigraphic architecture. *Geology* 44 (11), 931–934. https://doi.org/10.1130/G38158.1.

Kane, I.A., and Clare, M., 2018. Dispersion, Accumulation and the Ultimate Fate of Microplastics in Deep-Marine Environments: A Review and Future Directions. *Frontiers in earth science*, 7, 80 https://doi.org/10.31223/osf.io/ahjes.

Kane, I. A., McCaffrey, W. D., and Peakall, J., 2008. Controls on sinuosity evolution within submarine channels. *Geology*, 36(4), 287-290. https://doi.org/10.1130/G24588A.1.

Kim, W., Sheets, B. A., and Paola, C., 2010, Steering of experimental channels by lateral basin tilting, *Basin Research*, 22(3), 286– 301. https://doi.org/10.1111/j.1365-2117.2008.00418.x

Kneller, B. 2003. The influence of flow parameters on turbidite slope channel architecture. *Marine and Petroleum Geology*, 20(6-8), 901-910. https://doi.org/10.1016/j.marpetgeo.2003.03.001.

Komar, P. D. 1968. The channelized flow of turbidity currents with application to Monterey deep-sea fan channel. *Journal of Geophysical Research*, 74(18), 4544-4558. https://doi.org/10.1029/JC074i018p04544

Koneshloo, M., Aryana, S. A., Grana, D., and Pierre, J. W. 2017. A workflow for static reservoir modelling guided by seismic data in a fluvial system. *Mathematical Geosciences*, 49(8), 995-1020. http://doi.org/10.1007/s11004-017-9696-8.

Labourdette, R., and Bez, M. 2010. Element migration in turbidite systems: Random or systematic depositional processes?. *AAPG bulletin*, 94(3), 345-368. http://doi.org/10.1306/09010909035

De Leeuw, J., Eggenhuisen, J. T., & Cartigny, M. J., 2016. Morphodynamics of submarine channel inception revealed by new experimental approach. Nature communications, 7(1), 1-7. https://doi.org/10.1038/ncomms10886.

Lemay, M., 2018. *Transposition to the channelized submarine environment of a model of meandering fluvial systems in the view of reservoir modelling*. PhD thesis, MINES ParisTech – PSL University. Retrieved from these.fr. https://www.theses.fr/en/s157332.

Lemay, M., Ors, F., Grimaud, J., Rivoirard, J., & Cojan, I., 2019, September. Forward model applied to channelized turbidite systems: a case study of the Benin major valley fill. In *Petroleum Geostatistics 2019* (Vol. 2019, No. 1, pp. 1-5). European Association of Geoscientists & Engineers. https://doi.org/10.3997/2214-4609.201902223

Lemay, M., Grimaud, J.L., Cojan, I., Rivoirard, J., and Ors, F., 2020. Geomorphic variability of submarine channelized systems along continental margins: comparison with fluvial meandering channels *Marine and Petroleum Geology,* 115, p. 104295, https://doi.org/10.1016/j.marpetgeo.2020.104295

Limaye, A.B., Grimaud, J.L., Lai, S.Y., Foreman, B.Z., Komatsu, Y., and Paola, C., 2018. Geometry and dynamics of braided channels and bars under experimental density currents. *Sedimentology* 65, 1947–1972. https://doi.org/10.1111/sed.12453.

Lopez, S., 2003. *Modélisation de réservoirs chenalisés méandriformes: approche génétique et stochastique*. PhD thesis, Ecole des Mines de Paris. [In French]. Retrieved from theses.fr (http://www.theses.fr/2003ENMP1260).

Macauley, R. V., and Hubbard, S. M., 2013. Slope channel sedimentary processes and stratigraphic stacking, Cretaceous Tres Pasos Formation slope system, Chilean Patagonia. *Marine and Petroleum Geology*, 41, 146-162. https://doi.org/10.1016/j.marpetgeo.2012.02.004

Mayall, M., and O'Byrne, C. 2002. Reservoir prediction and development challenges in turbidite slope channels. *In Offshore Technology Conference*, 6-9 May 2002, Houston, Texas, USA.

McHargue, T., Pyrcz, M.J., Sullivan, M.D., Clark, J.D., Fildani, A., Romans, B.W., et al. 2011. Architecture of turbidite channel systems on the continental slope: patterns and predictions. *Marine and Petroleum Geology,* 28 (3), 728–743. https://doi.org/10.1016/j.marpetgeo.2010.07.008.

Mitchell, W. H., Whittaker, A. C., Mayall, M., Lonergan, L., and Pizzi, M. 2022. Quantifying structural controls on submarine channel architecture and kinematics. *Bulletin*, 134(3-4), 928-940. https://doi.org/10.1130/B36001.1

Morris, P. D., Sylvester, Z., Covault, J. A., & Mohrig, D. 2022 Channel Trajectories Control Deep-Water Stratigraphic Architecture. *The Depositional Record*. https://doi.org/10.1002/dep2.189

Nakajima, T., and Kneller, B. C. 2013. Quantitative analysis of the geometry of submarine external levees. *Sedimentology*, 60(4), 877-910. https://doi.org/10.1111/j.1365-3091.2012.01366.x.

Parquer, M., Yan, N., Colombera, L., Mountney, N. P., Collon, P., and Caumon, G. 2020. Combined inverse and forward numerical modelling for reconstruction of channel evolution and facies distributions in fluvial meander-belt deposits. *Marine and Petroleum Geology*, 117, 104408. https://doi.org/10.1016/j.marpetgeo.2020.104409

Paull, C. K., Talling, P. J., Maier, K. L., Parsons, D., Xu, J., Caress, D. W., ... and Cartigny, M. J. 2018. Powerful turbidity currents driven by dense basal layers. *Nature communications*, 9(1), 1-8. https://doi.org/10.1038/s41467-018-06254-6

Peakall, J., McCaffrey, B., and Kneller, B., 2000. A process model for the evolution, morphology, and architecture of sinuous submarine channels. *Journal of Sedimentary Research* 70 (3), 434–448. https://doi.org/10.1306/2DC4091C-0E47-11D7-8643000102C1865D

Pirmez, C., and Imran, J., 2003. Reconstruction of turbidity currents in Amazon channel. *Marine and Petroleum Geology,* 20 (6–8), 823–848. https://doi.org/10.1016/j.marpetgeo.2003.03.005.

Savitzky, A., and Golay, M.J., 1964. Smoothing and differentiation of data by simplified least squares procedures. *Anal. Chem.* 36 (8), 1627–1638.

Schumer, R., Jerolmack, D., & McElroy, B. (2011). The stratigraphic filter and bias in measurement of geologic rates. *Geophysical Research Letters*, *38*(11). https://doi.org/10.1029/2011GL047118.

Seminara, G., 2006. Meanders. *Journal of fluid mechanics*, 554, 271-297. https://doi.org/10.1017/S0022112006008925

Skene, K.I., Piper, D.J., and Hill, P.S., 2002. Quantitative analysis of variations in depositional sequence thickness from submarine channel levees. *Sedimentology* 49 (6), 1411–1430. https://doi.org/10.1046/j.1365-3091.2002.00506.x.

Smith, C. E. 1998. modelling high sinuosity meanders in a small flume. *Geomorphology*, 25(1-2), 19-30. https://doi.org/10.1016/S0169-555X(98)00029-4.

Straub, K.M., and Mohrig, D., 2008. Quantifying the morphology and growth of levees in aggrading submarine channels. *Journal of Geophysical Research: Earth Surface* 113 (F3). https://doi.org/10.1029/2007JF000896

Sylvester, Z., & Covault, J. A., 2016. Development of cutoff-related knickpoints during early evolution of submarine channels. Geology, 44(10), 835-838. https://doi.org/10.1130/G38397.1

Sylvester, Z., Durkin, P., & Covault, J. A,. 2018. High curvatures drive river meandering. Geology, 47(3), 263-266. https://doi.org/10.1130/G45608.1

Sylvester, Z., Durkin, P. R., Hubbard, S. M., and Mohrig, D., 2021. Autogenic translation and counter point bar deposition in meandering rivers. *Bulletin*, 133(11-12), 2439-2456. https://doi.org/10.1130/B35828.1

Sylvester, Z., Pirmez, C., and Cantelli, A., 2011. A model of submarine channel-levee evolution based on channel trajectories: implications for stratigraphic architecture. *Marine and Petroleum Geology,* 28 (3), 716–727. https://doi.org/10.1016/j.marpetgeo.2010.05.012.

Tal, M., and Paola, C., 2010. Effects of vegetation on channel morphodynamics: results and insights from laboratory experiments. *Earth Surface Processes and Landforms*, 35(9), 1014-1028. https://doi.org/10.1002/esp.1908.

Traer, M.M., Fildani, A., Fringer, O., McHargue, T., and Hilley, G.E., 2018. Turbidity current dynamics: 2. Simulating flow evolution toward equilibrium in idealized channels. *Journal of Geophysical Research: Earth Surface* 123 (3), 520–534. https://doi.org/10.1002/2017JF004202

Dijk, W. M., Lageweg, W. I., and Kleinhans, M. G., 2012. Experimental meandering river with chute cutoffs. *Journal of Geophysical Research: Earth Surface*, 117(F3). https://doi.org/10.1029/2011JF002314.

Wiles, E., Green, A., Watkeys, M., and Jokat, W., 2017. The Zambezi Channel: a new perspective on submarine channel evolution at low latitudes. *Geomorphology* 286, 121–132. https://doi.org/10.1016/j.geomorph.2017.02.014.

Willems, C., Vondrak, A., Mijnlieff, H., Donselaar, M., and Van Kempen, B., 2020. Geology of the Upper Jurassic to Lower Cretaceous geothermal aquifers in the West Netherlands Basin – an overview. *Netherlands Journal of Geosciences*, 99, E1. https://doi:10.1017/njg.2020.1

Figure Captions

Figure 1: Representative stratigraphic architectures along the Benin-major Canyon fill from seismic 2D sections (after Deptuck et al. 2007) showing complex channel stacking pattern through time: translation then aggradation in one direction (a) or two-ways migration (b). Black reflectors correspond to channelized deposit records.

Figure 2: Plan view (a) and cross-section (b) views showing migration and aggradation processes between two consecutive time steps

Figure 3: 3D aerial view of the simulated domain (a) and cross-sections perpendicular to flow (b) of the FLUMY simulation. Facies distribution and channelized deposits stacking patterns are given by the facies colour code. Cross-sections are looking downstream.

Figure 4: The three selected final simulated centrelines among the 9 simulated channel belts and location of the extracted bend cross-sections. Bends 8.6, 2.9, 6.5, and 6.14 are zoomed in Figure 5, and the cross-sections are shown in Figure 6. Bend colour code: blue-positive curvature, red-negative curvature.

Figure 5: Illustration of the phases of bend evolution during the simulation using 10 centrelines over the 40 extracted from channel-belts evolution (a, c, f, i). See Figure 4 for bend location. Cross-sections can intersect several successive bends which results in successive phases of channel point migration directions. The section crossing bend 6.5 recorded a single phase of channel points migration (b), the sections crossing bends 8.6 (d, e) and 6.14 (g, h) recorded two migration phases, and the section cross bend 2.9 recorded three migration phases (j, k, l).

Figure 6: Cross-sections of the four types of channel stacking patterns based on channel apparent trajectory: (a) type 1 (23%), (b) type 2 (11%), (c) type 3 (52%), (d) type 4 (14%). Phases correspond to change of apparent migration. Changes of channel colour materialise a change of the bend intersecting the cross-section. Channels in blue (red) means that curvature at the given channel point is positive (negative). See Figure 4 for bend location.

Figure 7: Violin-plots of belt-averaged bend total migration path according to stacking pattern types and normalised by channel width: (a) total migration Mig_{norm}, (b) migration orthogonal to the cross-section $D_{1,\,norm}$, and (c) migration parallel to the cross-section $D_{2,norm}$. The width of the boxes is proportional to the number of measurement points. Min: minimum, Q1: 1st quartile, Med: median, Q3: 3rd quartile, Max: maximum.

Figure 8: Violin-plots of horizontal (a, b) *Lc* and vertical (c) *La* channel displacements recorded on cross-sections according to whole path -subscript *w*- (a) or final path -subscript *f*- (b, c), and to stacking pattern types. *Lc* and La were normalised according to channel width *B* and depth *H*, respectively. $La_{w,\,norm}$ is constant for all types (see section 2.2.4). The width of the boxes is proportional to the number of measurement points. Min: minimum, Q1: 1st quartile, Med: median, Q3: 3rd quartile, Max maximum.

Figure 9: Comparison (cross-plot) between belt-averaged mobility numbers measured on simulated geological cross-sections $\mu_f = Lc_{f,\,norm}/La_{f,\,norm}$ (a) and $\mu_w = Lc_{w,\,norm}/La_{w,\,norm}$ (b) and from average bend migration path measurements M_{bend}. The corresponding distributions are also shown in violin-plots according to stacking pattern types (c, d, e). Violin-plot displays the distributions of the ratios

M_{bend}/μ_w and M_{bend}/μ_f according to stacking pattern types (f). The width of the boxes is proportional to the number of measurement points. Min: minimum, Q1: 1st quartile, Med: median, Q3: 3rd quartile, Max: maximum.

Figure 10: Comparison of average bend migration with the corresponding record for the four selected cross-sections between each consecutive centreline. Dashed and solid lines correspond to recorded leftward and rightward -i.e., migration phases- channel displacements in cross-sections of Figure 6, respectively. Migration colour code: red, negative curvature and blue: positive curvature.

Figure 11: Model of autogenic meander kinematics in the case of a downstream migrating meander bend (a) and recorded sigmoidal channel trajectory on 2D cross-section (b). Apparent migration increases (decreases) while the channel becomes more and more parallel (orthogonal) to the section.

Table Caption

Table 1: Median errors and median relative errors (in brackets) between recorded mobility number and bend mobility number according to the channel stacking pattern type.

	Type 1	Type 2	Type 3	Type 4
μ_w - M_{bend}	0.43 (+45%)	0.28 (+29%)	0.001 (0.1%)	-0.08 (-10%)
μ_f - M_{bend}	0.43 (+45%)	0.49 (+49%)	0.73 (+88%)	0.96 (+133%)

Table 1

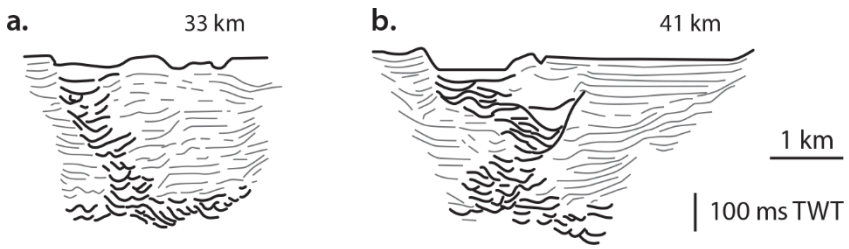

Figure 1

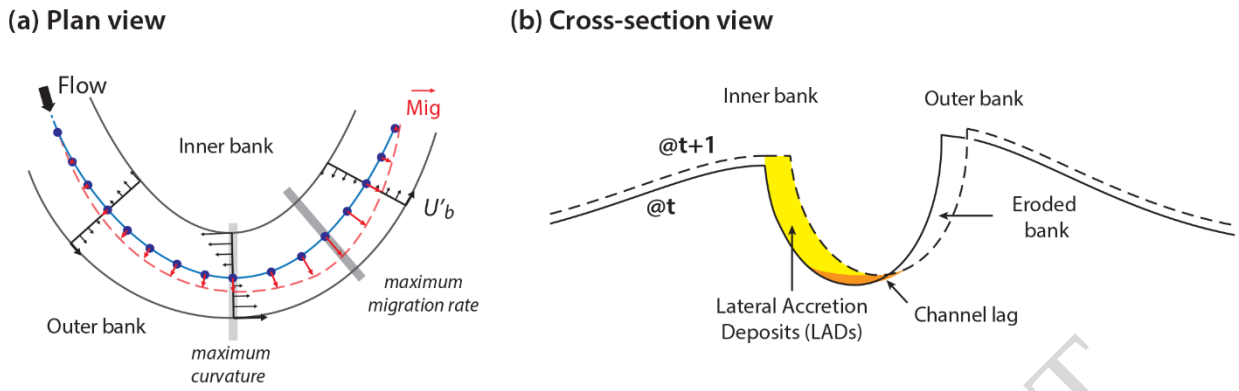

Figure 2

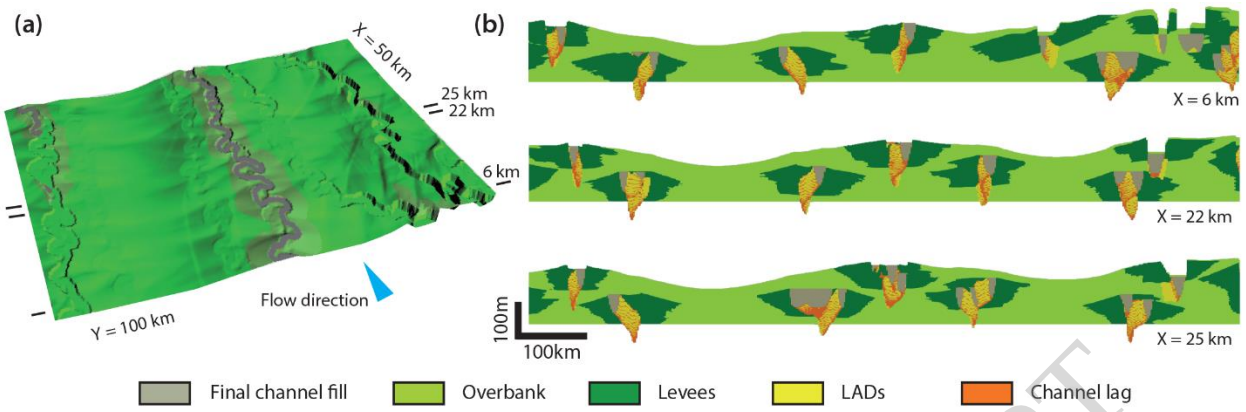

Figure 3

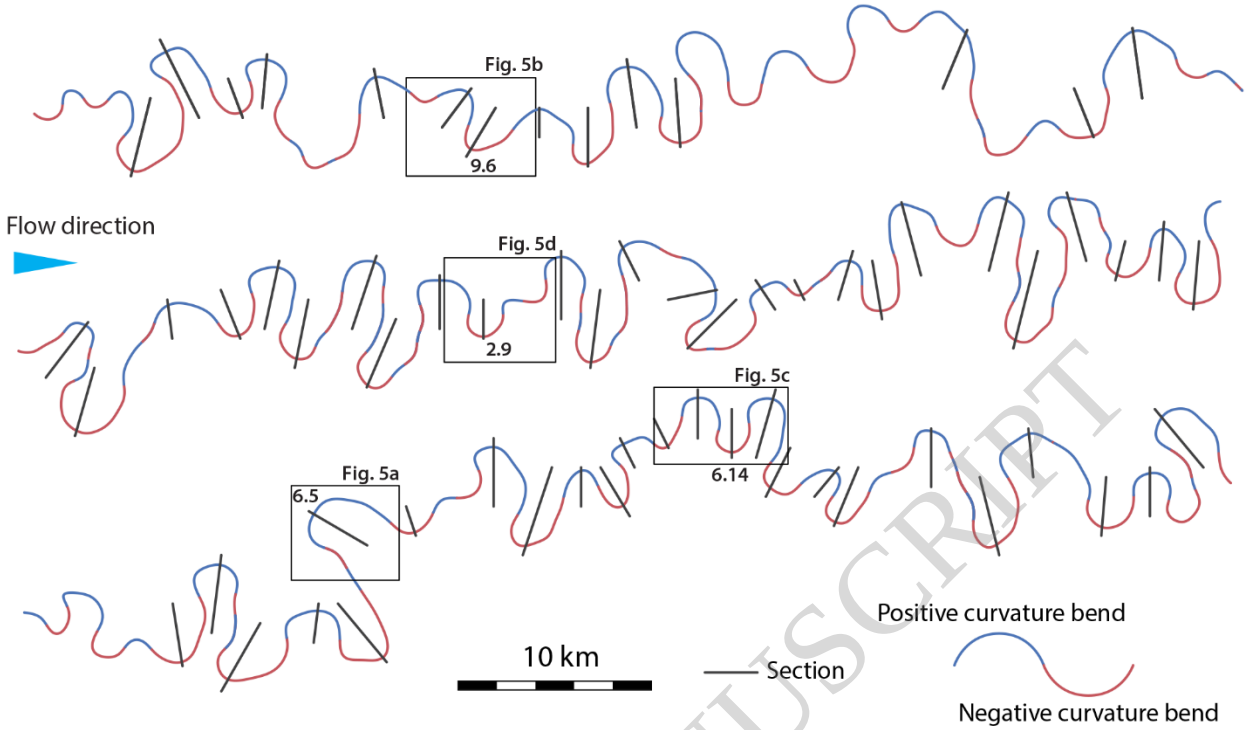

Figure 4

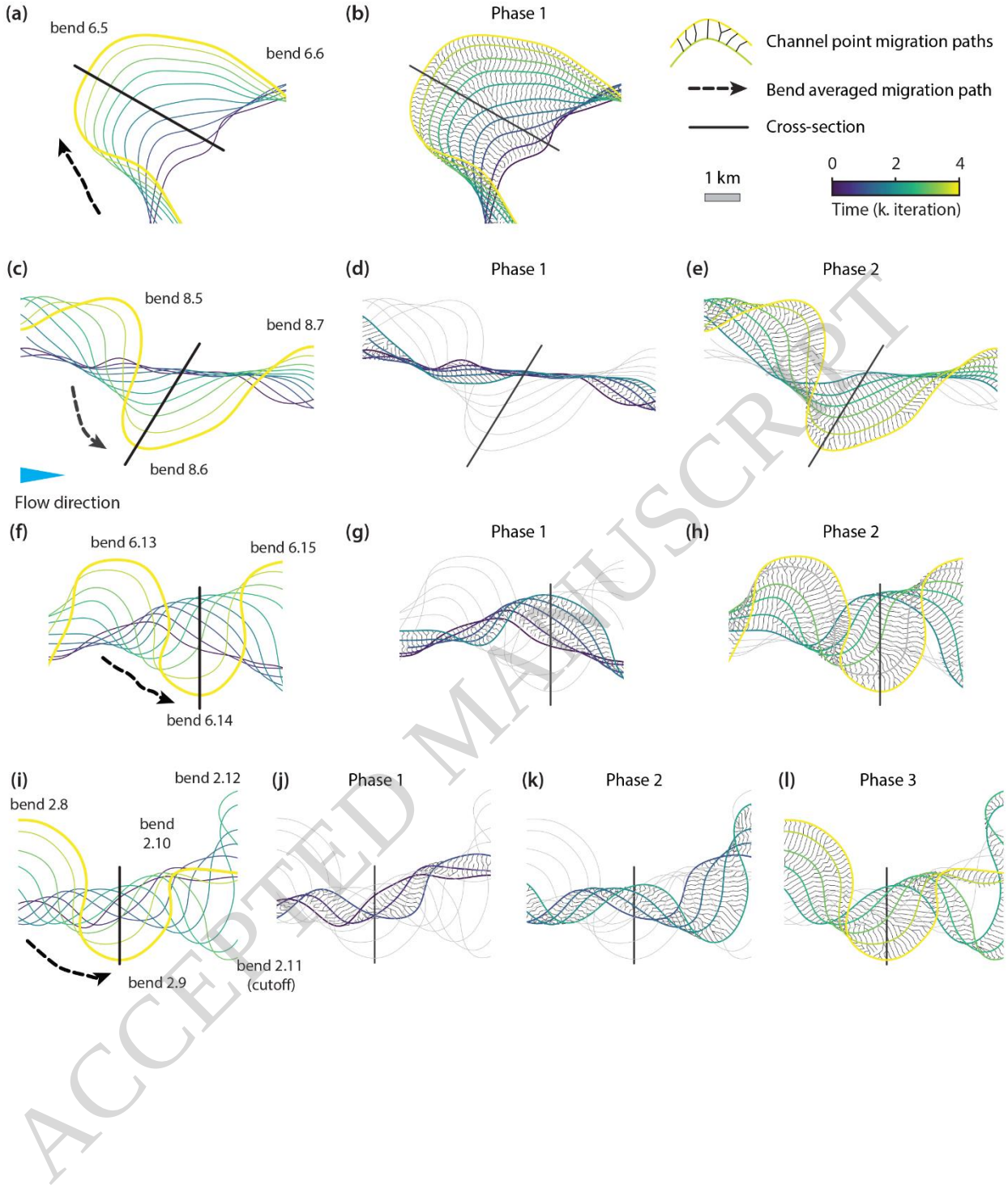

Figure 5

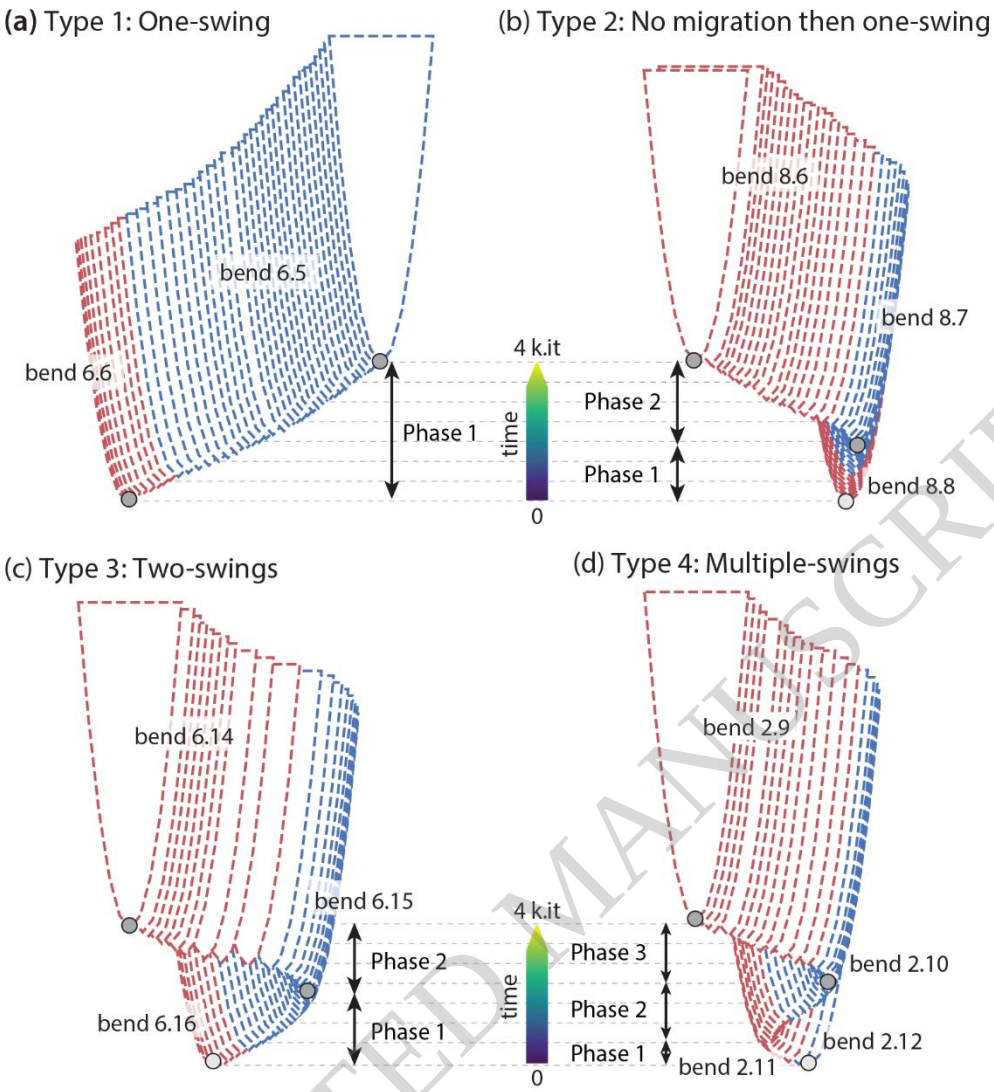

Figure 6

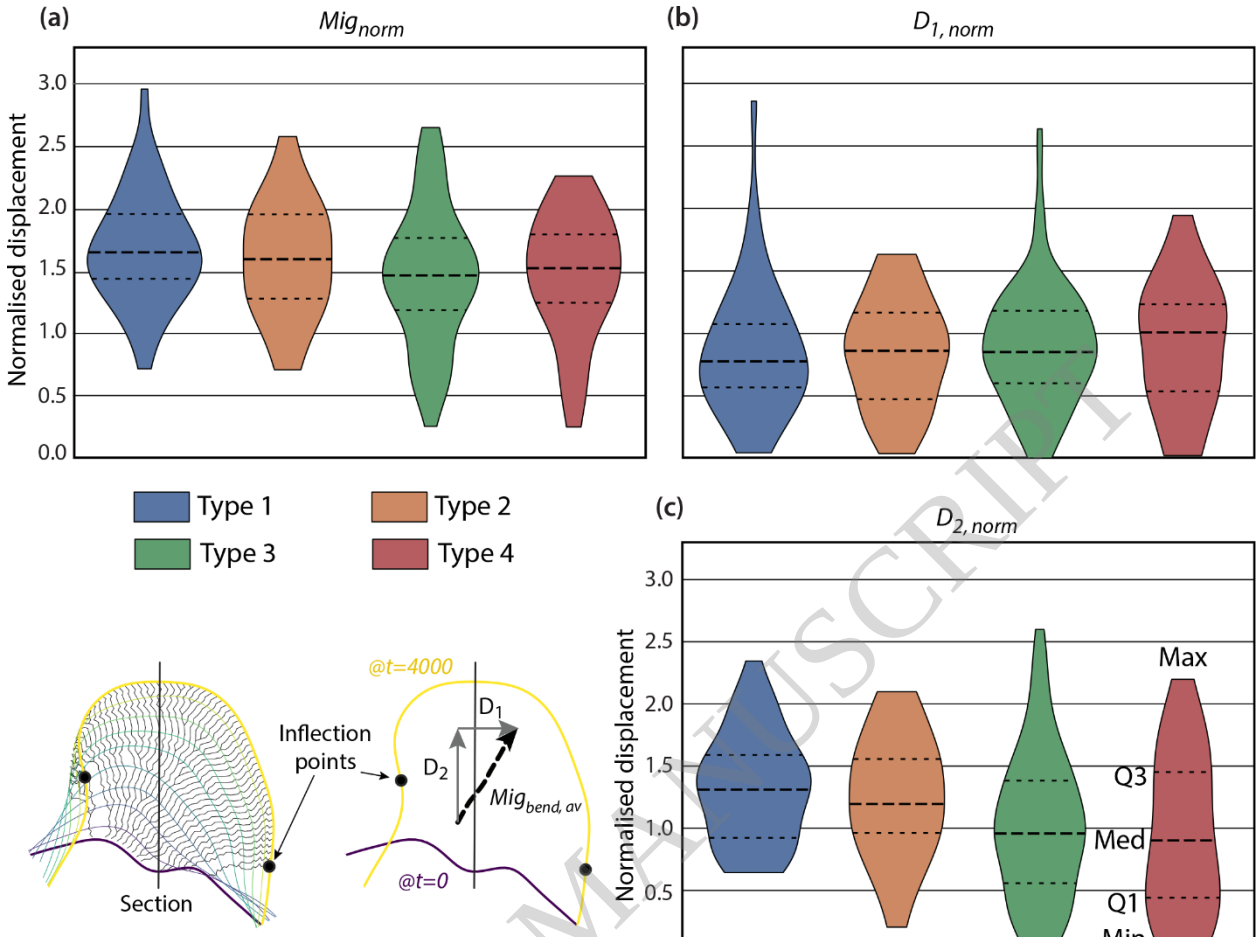

Figure 7

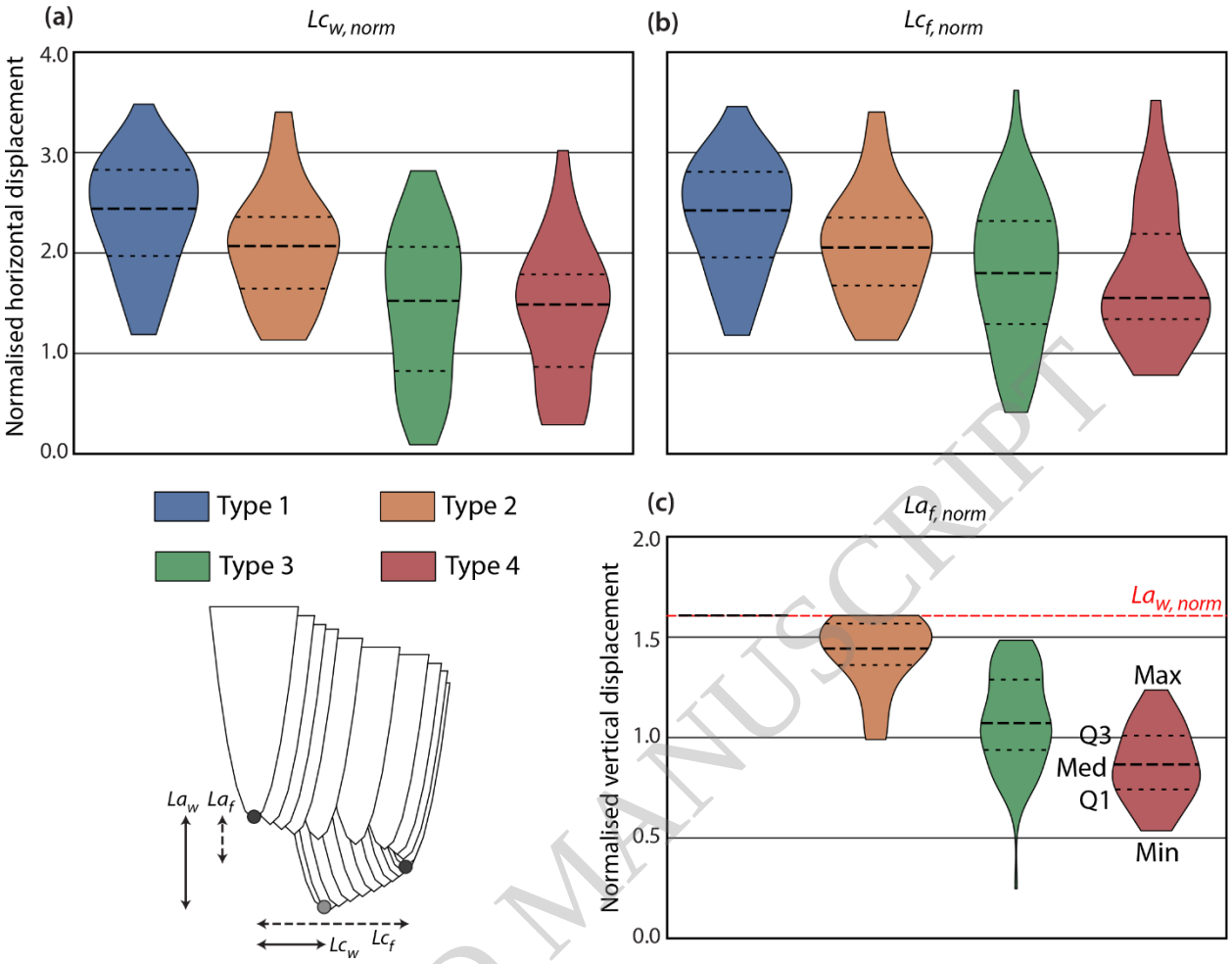

Figure 8

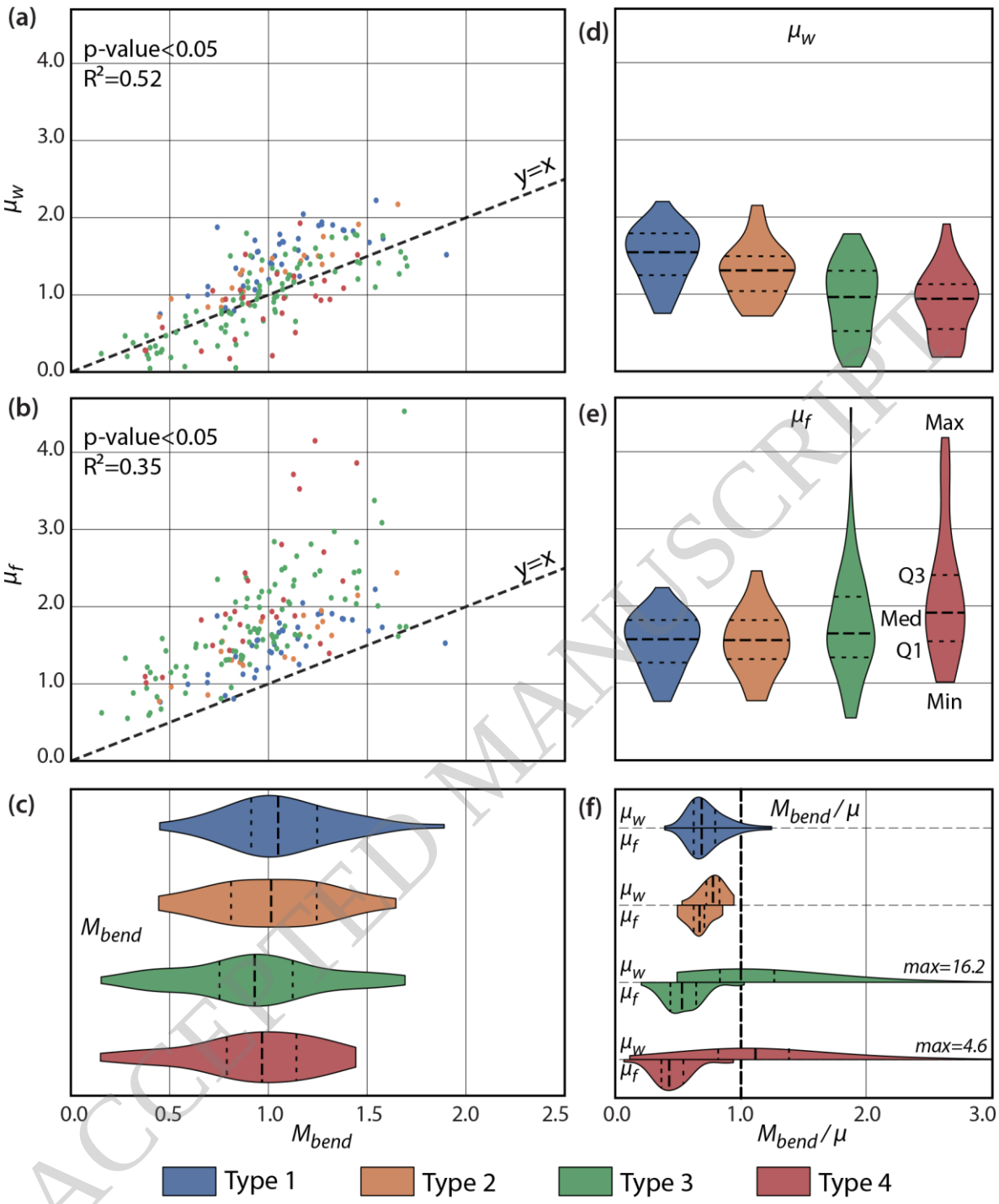

Figure 9

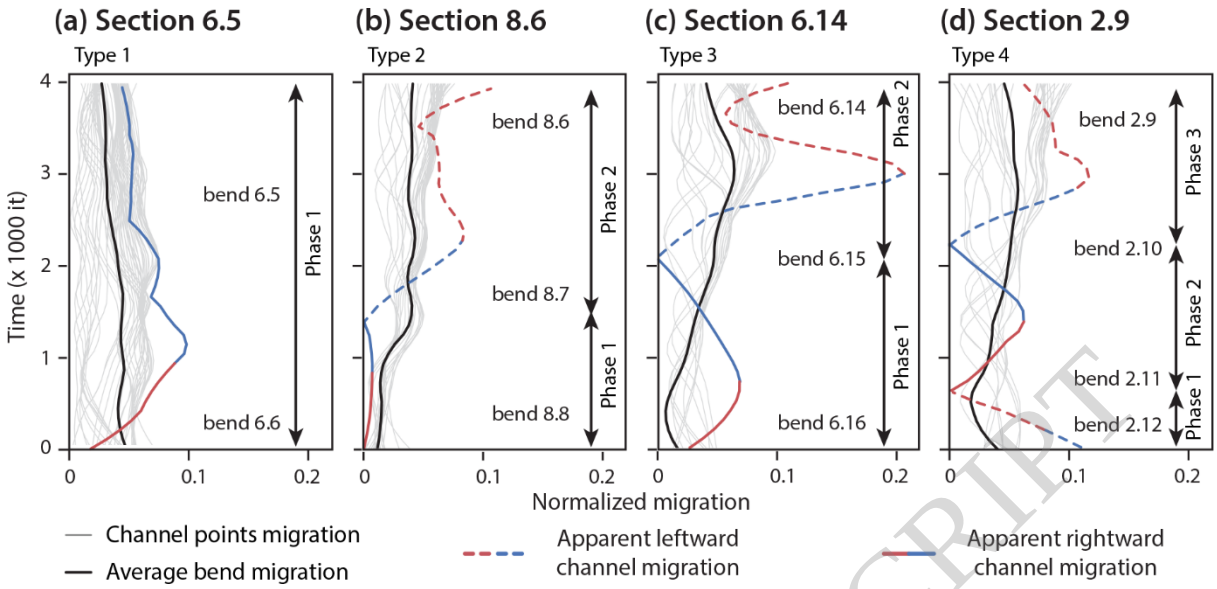

Figure 10

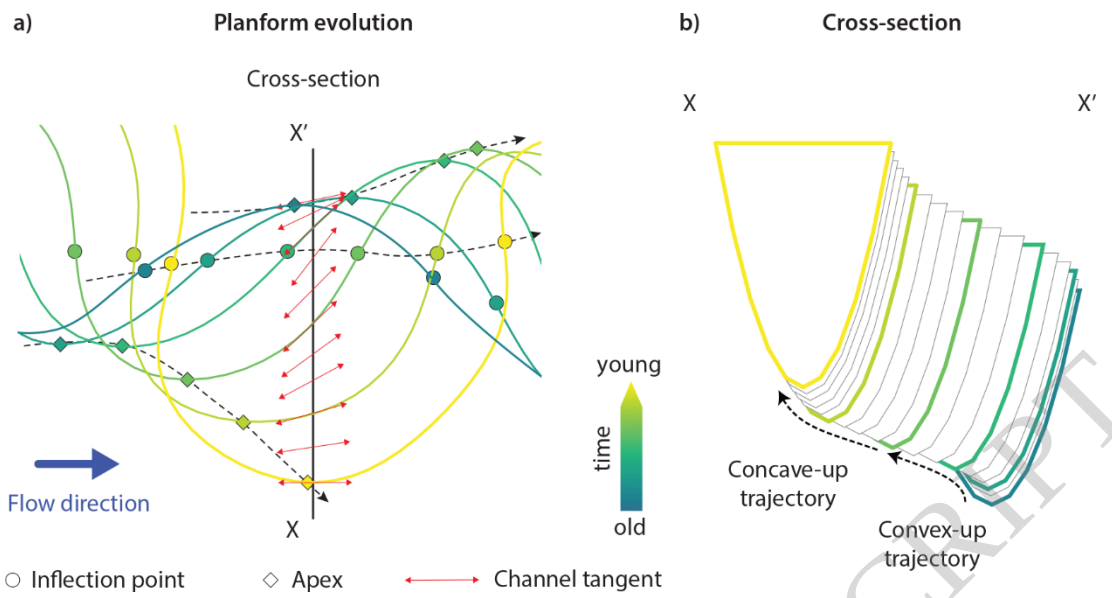

Figure 11